

# Analysis of Energy Level Structure and Excited-State Dynamics in a $\text{Sm}^{3+}$ Complex with Soft-Donor Ligands: $\text{Sm}(\text{Et}_2\text{Dtc})_3(\text{bipy})$

X. Y. Chen,<sup>†</sup> M. P. Jensen, and G. K. Liu\*

Chemistry Division, Argonne National Laboratory, Argonne, Illinois 60439

Received: April 1, 2005; In Final Form: May 9, 2005

Using both laser-excited fluorescence and optical absorption methods, we have determined 57 crystal-field (CF) energy levels of  $\text{Sm}^{3+}$  in crystals of  $\text{Sm}(\text{Et}_2\text{Dtc})_3(\text{bipy})$ . The analysis of the energy levels is based on a model Hamiltonian consisting of both free-ion and CF terms. The CF modeling of the experimental energy levels yielded physically reasonable Hamiltonian parameters with a final rms deviation of  $17.3 \text{ cm}^{-1}$ . In comparison with  $\text{Sm}^{3+}$  in other hosts, the CF splitting of  $\text{Sm}^{3+}$  in the lattice of  $\text{Sm}(\text{Et}_2\text{Dtc})_3(\text{bipy})$  is rather weak. The observed fluorescence decay of the  $^4\text{G}_{5/2}$  manifold is single-exponential, with a lifetime of  $24.5 \mu\text{s}$ , indicating only one site of  $\text{Sm}^{3+}$  in the lattice. According to the Judd–Ofelt theory, values of three intensity parameters were obtained ( $\Omega_{2,4,6} = 1.57, 2.65, \text{ and } 3.65$ , in units of  $10^{-20} \text{ cm}^{-1}$ ). The calculated branching ratios for transitions from the  $^4\text{G}_{5/2}$  manifold are in agreement with experimental values. The calculated radiative lifetime of the  $^4\text{G}_{5/2}$  manifold is  $3.24 \text{ ms}$ , and the corresponding fluorescence quantum efficiency is only  $0.75\%$ . Efficient multiphonon relaxation processes induced by the localized high-frequency vibrational modes in the bipyridyl group may lead to the extremely low quantum efficiency observed. The thermal line broadening and shifts of the  $^4\text{G}_{5/2}(1) \rightarrow ^6\text{F}_{1/2}$  transition were observed and fitted very well by the McCumber–Sturge equations with an assumption of Raman phonon scattering processes as the leading relaxation mechanism. The Debye temperature for this crystal is predicted to be  $350 \text{ K}$ .

## I. Introduction

The great chemical similarity of the trivalent lanthanide (Ln) and actinide (An) cations often fails in complexes with ligands containing donor atoms, such as N, S, or Cl, that are soft compared to oxygen. This effect is generally attributed to a modest enhancement of covalency in the An–ligand bonds as compared to the lanthanides, which produces thermodynamically more stable An–soft-donor complexes.<sup>1</sup> Although the greater affinity of  $\text{An}^{3+}$  ions for soft-donor ligands makes it possible to chemically separate  $\text{Ln}^{3+}$  from  $\text{An}^{3+}$  in nuclear waste management, the origin and magnitude of the covalent contribution to f–element bonding is not quantitatively understood and is a matter of continuing investigation. Recently, structural<sup>2–5</sup> and thermodynamic<sup>6,7</sup> approaches have been used to compare the covalency in  $\text{Ln}^{3+}$  and  $\text{An}^{3+}$  complexes with thio-substituted dialkylphosphinate or with polycyclic aromatic amine ligands, but detailed experimental studies of the electronic interactions in these types of soft-donor complexes are rare.

Although they are not suitable for practical chemical separations, mixed-ligand coordination compounds of the lanthanides,  $\text{Ln}(\text{Et}_2\text{Dtc})_3(\text{bipy})$ , which have the formula  $\text{Ln}_1\text{C}_{25}\text{H}_{38}\text{N}_5\text{S}_6$  ( $\text{Et}_2\text{Dtc} = N,N$ -diethyldithiocarbamate;  $\text{bipy} = 2,2'$ -bipyridyl), are excellent model compounds for initiating comprehensive spectroscopic studies of  $\text{Ln}^{3+}$  and  $\text{An}^{3+}$  soft-donor complexes because each central trivalent f–element ion is coordinated only by soft-donor atoms, six sulfur atoms from three bidentate  $\text{Et}_2\text{Dtc}$  ligands and two soft nitrogen atoms from a bidentate bipy ligand. Moreover, the synthesis of almost the entire series of

$\text{Ln}(\text{Et}_2\text{Dtc})_3(\text{bipy})$  ( $\text{Ln} = \text{La–Nd, Sm–Lu, Y}$ ) compounds<sup>8,9</sup> and the crystal and molecular structures of the  $\text{Pr}$ ,<sup>10</sup>  $\text{Sm}$ ,<sup>11</sup>  $\text{Eu}$ ,<sup>12</sup> and  $\text{Er}$ <sup>8</sup> complexes have been reported. Although the baricenters of some of the f–f transitions have been reported for the solution phase complexes of certain lanthanides,<sup>8</sup> no detailed spectroscopic study of this class of compounds has ever been reported.

The preparation of a series of trivalent lanthanide and actinide  $\text{M}(\text{Et}_2\text{Dtc})_3(\text{bipy})$  ( $\text{M} = \text{Ln}^{3+}, \text{An}^{3+}$ ) complexes will enable us to investigate the electronic properties of both the lanthanide ( $4f^N$ ) and actinide ions ( $5f^N$ ) systematically. We expect that the  $4f$  and  $5f$  ions will experience significant differences in the metal–ion–ligand interactions, leading to nonradiative relaxation, charge transfer, and structural distortions and that there will be systematic trends in the variation of bonding properties across these series of elements. The  $\text{Sm}^{3+}$  ion in  $4f^5$  electronic states with a fluorescence emitting state near  $560 \text{ nm}$  is an ideal case for characterizing the electronic structure and ion–ligand interactions. Detailed analysis of the energy level structure and excited-state dynamics in terms of fluorescence decay and energy transfer should provide primary information about the electronic interactions in f–element complexes with soft-donor ligands.

In this paper, we report the optical spectra and electronic structures of  $\text{Sm}^{3+}$  in  $\text{Sm}(\text{Et}_2\text{Dtc})_3(\text{bipy})$ . Our aim is to evaluate the spectroscopic parameters such as Judd–Ofelt (JO) intensity, radiative lifetime, and crystal-field (CF) parameters of the title compound. This work provides the foundation for a predictive understanding of the behavior of other members of this family of compounds and gives insights into the effect of covalency on the spectroscopic properties of f–element optical centers coordinated with soft-ligand atoms.

\* To whom correspondence should be addressed. E-mail: gkliu@anl.gov.

<sup>†</sup> Current address: Fujian Institute of Research on the Structure of Matter, Fuzhou, Fujian 350002, China.

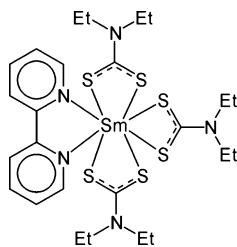


**Figure 1.** Schematic two-dimensional projection of the molecular structure of  $\text{Sm}(\text{Et}_2\text{Dtc})_3(\text{bipy})$ .

## II. Experimental Section

Single crystals of  $\text{Sm}(\text{Et}_2\text{Dtc})_3(\text{bipy})$  were synthesized from a 1:3:1 mixture of hydrated samarium perchlorate, diethylammonium diethyldithiocarbamate (98%, Aldrich), and 2,2'-bipyridine (99+%, Aldrich) in acetonitrile according to the procedure of Su et al.<sup>8</sup> The obtained single crystals were small (with a size of 0.1–0.2 mm), pale yellow, and air stable. The crystal structure of single crystals of  $\text{Sm}(\text{Et}_2\text{Dtc})_3(\text{bipy})$  has been reported by Varand et al.<sup>11</sup> Figure 1 shows a schematic 2D projection of the molecular structure in which the Sm atom lies inside a distorted dodecahedron formed by six S atoms of three cyclic bidentate diethyldithiocarbamate ligands lying at a distances of 2.807–2.908 Å and by two N atoms of the bipy molecule lying 2.614–2.616 Å away from the Sm atom.<sup>11</sup> The crystal belongs to space group  $P2_1/c$ , and the Sm atom occupies the lowest site symmetry of  $C_1$ .

To obtain the emission spectrum of the  $\text{Sm}^{3+}$  ion, we used an ultraviolet (UV) pulsed laser at 355 nm to pump the samples, which had been mounted on an Optistat bath cryostat (Oxford Instruments). To obtain the excitation spectrum, we used a pulsed dye laser (Lambda Physik, Scanmate 2EC), which provides a pulse width of 5 ns, a repetition rate of 10 Hz, and a tunable range from 480 to 550 nm, to pump the samples. The fluorescence emission was dispersed by a monochromator (SPEX 1704) at a spectral resolution of approximately 0.008 nm and detected with a cooled RCA C31034 photomultiplier. The signals were recorded using a gated boxcar (Stanford Research Systems, model SR250). The fluorescence decay measurements were performed using a digital storage oscilloscope (Tektronix TDS 680C). All of the measurements were performed from 77 K to room temperature (RT). The emission spectra have been calibrated based on the various grating and PMT efficiencies at different wavelengths.

To measure the absorption spectra, single crystals (about 10–15 wt %) were ground and pressed into a pellet with KBr powder. For quantitative calculations, a known amount of single crystals were dissolved in chloroform to give a  $6.8 \times 10^{-4}$  M Sm solution and the absorption spectrum was measured in a 5-cm path length cell. UV–visible(VIS)–infrared(IR) absorption spectra of samples were collected with a computer-controlled Cary-14 spectrophotometer (OLIS, Inc.) at RT.

## III. Results and Discussion

**A. Absorption Spectra.** The UV–Vis–IR absorption spectrum of  $\text{Sm}^{3+}$  in the  $\text{Sm}(\text{Et}_2\text{Dtc})_3(\text{bipy})$ –KBr pellet was recorded at room temperature. Figure 2a shows the UV–Vis absorption from the ground state. A broad and intense peak appears with its low energy shoulder at 390 nm, which is likely due to the  $\text{Sm}^{3+}$ –ligand CT absorption. In comparison with model calculations, seven weak peaks at wavelengths 533, 504, 491, 483, 477, 468, and 455 nm can be identified and attributed to the absorption from the  $^6\text{H}_{5/2}$  to  $^4\text{F}_{3/2}$ ,  $^4\text{G}_{7/2}$ ,  $^4\text{I}_{9/2}$ ,  $^4\text{M}_{15/2}$ ,  $^4\text{I}_{11/2}$ ,  $^4\text{I}_{13/2}$ , and  $^4\text{F}_{5/2}$  manifolds, respectively, as marked in Figure 2a.

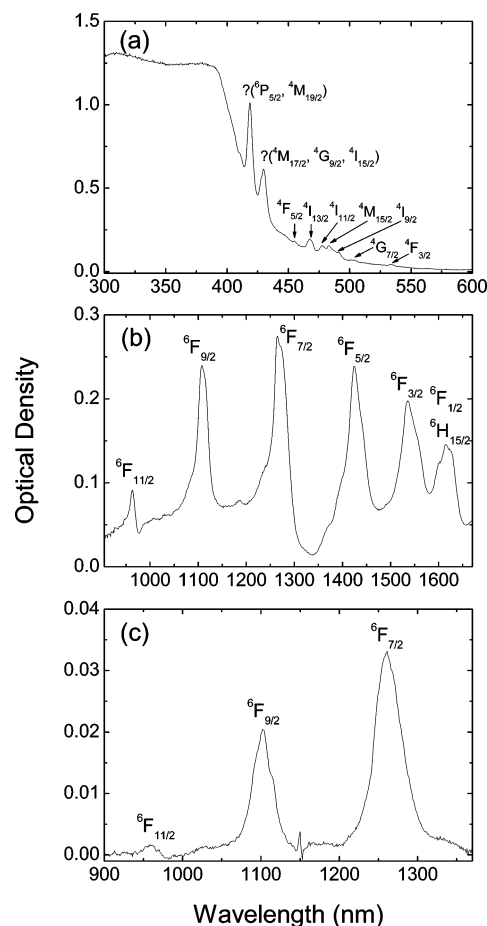


**Figure 2.** Room-temperature absorption spectra of  $\text{Sm}(\text{Et}_2\text{Dtc})_3(\text{bipy})$  crystals mixed in a KBr pellet in the spectral region of (a) 300–600 nm and (b) 900–1670 nm, respectively. Part of a room-temperature absorption spectrum of  $\text{Sm}(\text{Et}_2\text{Dtc})_3(\text{bipy})$  crystals in the chloroform solution is shown in (c). The corresponding absorption transition from the ground state is assigned for each peak.

These absorption transitions are nominally spin forbidden but weakly allowed as intermediate-coupling admixes into both the  $^6\text{H}_{5/2}$  and the terminal quartet's wave functions via spin–orbit interaction. Two intense peaks at 430 and 419 nm superimposed on the edge of CT absorption were tentatively attributed to the group of  $^4\text{M}_{17/2}$ ,  $^4\text{G}_{9/2}$ , and  $^4\text{I}_{15/2}$  and the group of  $^6\text{P}_{5/2}$  and  $^4\text{M}_{19/2}$ , respectively. Figure 2b shows absorption from 900 to 1670 nm, where six absorption bands centered at 964, 1108, 1264, 1424, 1535, and 1613 nm are transitions to  $^6\text{F}_{11/2}$ ,  $^6\text{F}_{9/2}$ ,  $^6\text{F}_{7/2}$ ,  $^6\text{F}_{5/2}$ ,  $^6\text{F}_{3/2}$ , and  $^6\text{F}_{1/2} + ^6\text{H}_{15/2}$ , respectively. Obviously, because of the spin-allowed nature of these transitions, the IR bands are much stronger than those in the visible region. Because these six bands are well resolved and isolated, we used them to perform the JO intensity calculation. For comparison, a part of the room-temperature absorption spectrum of  $\text{Sm}(\text{Et}_2\text{Dtc})_3(\text{bipy})$  crystals in chloroform solution is shown in Figure 2c.

Each of the bands in Figure 2a–c consists of several peaks from transitions between the ground state and the CF levels in the excited multiplet. The CF levels are not well resolved in the spectra mainly because of the instrument resolution and phonon broadening at room temperature. As will be discussed later in the paper, the unresolved CF bands also suggest that the CF splitting in these compounds is generally much smaller than that of  $\text{Sm}^{3+}$  in many other hosts. Although the CF levels of the multiplets could not be completely resolved from the room temperature absorption spectrum, some levels (or the centers of gravity) of the multiplets can be reliably determined. Those

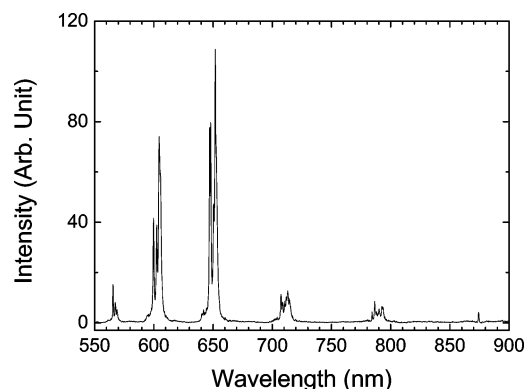


**Figure 3.** Emission spectrum of Sm<sup>3+</sup> in Sm(Et<sub>2</sub>Dtc)<sub>3</sub>(bipy) crystals at 77 K pumped by a pulsed laser at 355 nm. The spectrum shows the overall intensities of the transitions from the emitting state of <sup>4</sup>G<sub>5/2</sub> to <sup>6</sup>H<sub>5/2,7/2,9/2,11/2,13/2</sub> multiplets. The fluorescence was detected using a boxcar integrator that averaged the signal output from a cooled PMT. The boxcar time gate was 5 μs, and the delay from the pumping laser pulse was 10 μs.

levels play a very important role in correctly determining the free-ion (FI) parameters. Specifically, the positions of <sup>4</sup>F<sub>3/2</sub>, <sup>4</sup>G<sub>7/2</sub>, and <sup>4</sup>I<sub>9/2</sub> in Figure 2a are consistent with the results obtained from the laser excitation spectra, and the positions of <sup>6</sup>F<sub>3/2</sub>, and <sup>6</sup>F<sub>1/2</sub> in Figure 2b are consistent with the corresponding levels obtained from the emission spectra.

**B. Emission Spectra.** As noted above, the CF splitting of Sm<sup>3+</sup> electronic energy levels in Sm(Et<sub>2</sub>Dtc)<sub>3</sub>(bipy) is relatively weak and not resolved in the absorption spectrum. To obtain more detailed information, we conducted laser-excited luminescence studies. Figure 3 shows the emission spectrum of the Sm(Et<sub>2</sub>Dtc)<sub>3</sub>(bipy) crystals from 550 to 900 nm at 77 K when pumped by a pulsed Nd:YAG laser at 355 nm. Note that the sample has a large absorption cross section at 355 nm because of the Sm<sup>3+</sup>–ligand charge-transfer (CT) absorption, and no emission lines shorter than 550 nm were observed. The emission spectrum of Sm<sup>3+</sup> consists of transitions from the <sup>4</sup>G<sub>5/2</sub> excited state to the lower energy levels of <sup>6</sup>H<sub>J</sub> (*J* = 5/2, 7/2, 9/2, 11/2, 13/2, and 15/2) and <sup>6</sup>F<sub>J</sub> (*J* = 1/2 and 3/2).

Because of the Kramers degeneracy, the low-temperature emission pattern should consist of 3, 4, 5, 6, 7, 8, 1, and 2 lines, respectively, for each aforementioned manifold when Sm<sup>3+</sup> ions occupy a low-symmetry site in the crystalline lattice. The observed emission pattern agrees with the expected degeneracy, indicating that Sm<sup>3+</sup> ions indeed occupy a single site in this crystal. The sharp characteristic emission lines for the above groups are enlarged for analysis in Figure 4a–e, respectively. In Figure 4a, we are able to identify all of the emission transitions from the lowest CF level of <sup>4</sup>G<sub>5/2</sub> (hereafter referred to as <sup>4</sup>G<sub>5/2</sub>(1)) to the ground-state manifold, <sup>6</sup>H<sub>5/2</sub>, and to the first excited manifold, <sup>6</sup>H<sub>7/2</sub>. The energy level of <sup>4</sup>G<sub>5/2</sub>(1) is assigned at 17 687 cm<sup>−1</sup>. In Figure 4b–d, all of the emission lines arising from <sup>4</sup>G<sub>5/2</sub>(1) to <sup>6</sup>H<sub>7/2</sub>, <sup>6</sup>H<sub>9/2</sub>, and <sup>6</sup>H<sub>11/2</sub> manifolds can also be clearly identified. In Figure 4e, the exceptionally strong line was ascribed to the hypersensitive transition to <sup>6</sup>F<sub>1/2</sub>, whereas the weak near-IR peaks at lower energies were due to transitions to <sup>6</sup>H<sub>15/2</sub> and <sup>6</sup>F<sub>3/2</sub>. The assignment of the <sup>6</sup>F<sub>1/2</sub> level was also confirmed in the absorption spectra. One common feature in Figure 4a–e is that some weak sidebands accompanying the stronger CF lines, marked by arrows in the figure, are always observed at higher energies in the emission spectrum. These sidebands represent hot band transitions originating from the upper two CF levels of <sup>4</sup>G<sub>5/2</sub>, which may be lightly populated even at 77 K. Because only one line was observed for the

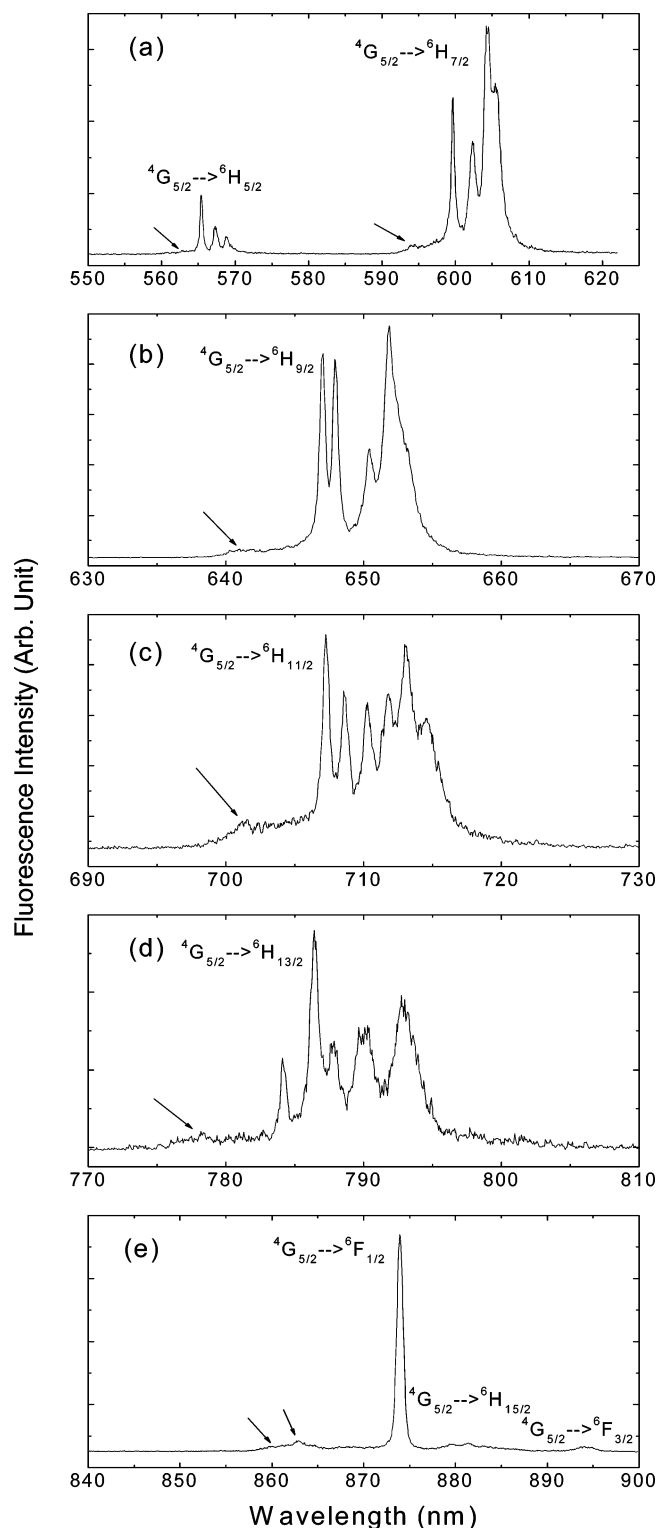


**Figure 4.** High-resolution emission spectra of Sm<sup>3+</sup> in Sm(Et<sub>2</sub>Dtc)<sub>3</sub>(bipy) crystals in the spectral region of (a) 550–625 nm; (b) 630–670 nm; (c) 690–730 nm; (d) 770–810 nm; (e) 840–900 nm, respectively. They were measured at 77 K with the same time delay and gate as those in Figure 2. Lines marked by arrows are hot bands originating from the upper CF levels of excited state <sup>4</sup>G<sub>5/2</sub>.

<sup>4</sup>G<sub>5/2</sub>(1) → <sup>6</sup>F<sub>1/2</sub> transition at 77 K, the hot band structures arising from the upper two CF levels of <sup>4</sup>G<sub>5/2</sub> can be resolved in Figure 4e. The positions of the upper CF levels of <sup>4</sup>G<sub>5/2</sub> thus can be established at 145 and 187 cm<sup>−1</sup>, respectively, above the lowest level. The observed energy levels corresponding to the above groupings are summarized in Table 1, where they are compared

**TABLE 1: Energy Levels of Sm<sup>3+</sup> in the Sm(Et<sub>2</sub>Dtc)<sub>3</sub>(bipy) Crystal at 77 K**

multiplet	energy (cm <sup>-1</sup> )		$\Delta E$ (cm <sup>-1</sup> ) <sup>a</sup>	multiplet	energy (cm <sup>-1</sup> )		$\Delta E$ (cm <sup>-1</sup> ) <sup>a</sup>	multiplet	energy (cm <sup>-1</sup> )		$\Delta E$ (cm <sup>-1</sup> ) <sup>a</sup>
	exp	fit			exp	fit			exp	fit	
<sup>6</sup> H <sub>5/2</sub>	0	16.5	16.5	<sup>4</sup> M <sub>15/2</sub>		20 543.5		<sup>4</sup> F <sub>7/2</sub>		24 712.7	
	61.1	69.6	8.5			20 563.7				24 713.1	
	108.1	120.2	12.1			20 586.0				24 724.5	
<sup>6</sup> H <sub>7/2</sub>	1010.8	1010.7	-0.1			20 598.7		<sup>4</sup> K <sub>11/2</sub>		24 742.1	
	1084.4	1060.2	-24.2			20 617.0	-4.0			24 857.4	
	1140.9	1147.2	6.3			20 656.7	-32.3			24 875.2	
<sup>6</sup> H <sub>9/2</sub>	1169.7	1187.0	17.3			20 722.2	16.2			24 902.9	
	2230.4	2209.3	-21.1			20 734.0				24 908.0	
	2252.2	2250.4	-1.8			20 816.0				24 912.2	
<sup>6</sup> H <sub>11/2</sub>	2310.7	2324.6	13.9	<sup>4</sup> I <sub>11/2</sub>		20 878.5				24 919.6	
	2345.3	2338.5	-6.8			20 899.7					
	2364.5	2372.7	8.2			20 913.9					
<sup>6</sup> H <sub>13/2</sub>	3544.7	3531.7	-13.0			20 964.6	20.6				
	3571.8	3550.0	-21.8			21 003.6					
	3604.4	3620.6	16.2			21 348.5					
<sup>6</sup> H <sub>15/2</sub>	3635.1	3638.2	3.1	<sup>4</sup> I <sub>13/2</sub>		21 370.9					
	3659.7	3646.4	-13.3			21 384.0					
	3689.2	3697.5	8.3			21 385.1	-2.9				
<sup>6</sup> F <sub>1/2</sub>	4931.6	4929.5	-2.1			21 412.2					
	4967.9	4965.5	-2.4			21 433.4					
	4990.2	4981.8	-8.4			22 006.7	22.7				
<sup>6</sup> H <sub>15/2</sub>	5020.4	5010.4	-10.0	<sup>4</sup> F <sub>5/2</sub>		22 023.5					
	5029.4	5014.3	-15.1			22 039.4					
	5069.8	5062.0	-7.8			22 345.8					
<sup>6</sup> F <sub>3/2</sub>	5082.8	5082.3	-0.5	<sup>4</sup> M <sub>17/2</sub>		22 351.5					
	6244.7	6251.8	7.1			22 367.5					
	6318.1	6338.3	20.2			22 375.4					
<sup>6</sup> F <sub>5/2</sub>	6341.6	6370.1	28.5			22 383.9					
	6362.7	6370.4	7.7			22 401.9					
	6406.2	6376.8	-29.4			22 409.7					
<sup>6</sup> F <sub>7/2</sub>		6449.3				22 419.6					
		6504.9	6.3			22 459.7					
		6511.3	0.9			22 579.6					
<sup>6</sup> F <sub>9/2</sub>		6523.8		<sup>4</sup> G <sub>9/2</sub>		22 603.8					
		6553.8				22 650.9					
		6586.8				22 661.1					
<sup>6</sup> F <sub>11/2</sub>		7000.7				22 708.5					
		7003.4				22 762.2					
		7021.8				22 769.8					
<sup>6</sup> F <sub>13/2</sub>		7832.1		<sup>4</sup> I <sub>15/2</sub>		22 772.7					
		7847.6				22 778.5					
		7869.0				22 815.3					
<sup>6</sup> F <sub>15/2</sub>		7905.6				22 830.0					
		8984.8				22 862.7					
		9027.8				22 867.8					
<sup>6</sup> F <sub>17/2</sub>		9029.3		<sup>6</sup> P <sub>5/2</sub>		23 642.3					
		9056.6				23 689.2					
		9062.5				23 718.0					
<sup>6</sup> F <sub>19/2</sub>		10 385.0		<sup>4</sup> M <sub>19/2</sub>		23 821.4					
		10 387.6				23 823.2					
		10 403.9				23 858.7					
<sup>4</sup> G <sub>5/2</sub>		10 406.5				23 870.2					
		10 427.9				23 884.7					
		10 456.2				23 889.5					
<sup>4</sup> G <sub>7/2</sub>		17 686.9				23 930.2					
		17 832.2				23 937.0					
		17 835.9				23 945.4					
<sup>4</sup> F <sub>3/2</sub>		17 873.9				24 010.6					
		18 751.2				24 010.6					
		18 743.4				24 367.8					
<sup>4</sup> G <sub>9/2</sub>		18 772.3		<sup>4</sup> L <sub>13/2</sub>		24 371.6					
		18 748.8				24 375.8					
		19 858.1				24 400.0					
<sup>4</sup> I <sub>9/2</sub>		19 907.3				24 401.8					
		19 932.2				24 413.6					
		19 956.8				24 413.9					
<sup>4</sup> I <sub>11/2</sub>		19 981.8				24 530.5					
		20 319.1				24 724.5					
		20 354.7									
<sup>4</sup> I <sub>13/2</sub>		20 372.9									
		20 369.4									
		20 441.2									
<sup>4</sup> I <sub>15/2</sub>		20 455.1									
		20 466.3									

<sup>a</sup> Energy difference,  $\Delta E = E_{\text{fit}} - E_{\text{exp}}$ .

to the results obtained from the CF fitting. Probing fluorescence emission in the IR region to detect crystal-field splitting of the <sup>6</sup>F<sub>J</sub> is possible. However, based on the intensity calculation to be discussed in Section V, the intensity of these transitions is

weak. As shown in Figure 4e, CF splitting cannot be clearly resolved from the weak bands of multiplets <sup>6</sup>H<sub>15/2</sub> and <sup>6</sup>F<sub>3/2</sub>.

Figure 5 shows the fluorescence decay of the <sup>4</sup>G<sub>5/2</sub>–<sup>6</sup>H<sub>9/2</sub> transition at 647.8 nm measured following the 355-nm excita-



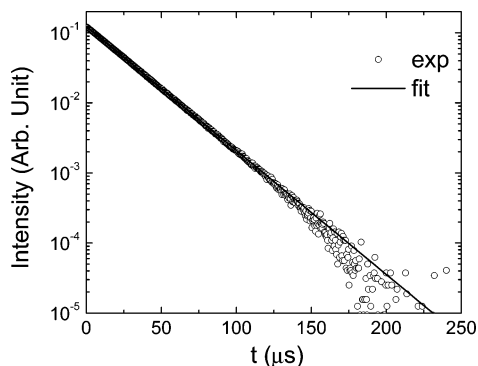


**Figure 5.** Decay of fluorescence emission from the  $^4G_{5/2}$  state of  $Sm^{3+}$  in  $Sm(Et_2Dtc)_3(bipy)$  crystals at 77 K. The fluorescence was monitored at 647.8 nm and pumped by a pulsed laser at 355 nm. The solid curve results from a monoexponential fitting to the experimental data.

tion. The fluorescence lifetime,  $24.53 \pm 0.01 \mu s$  at 77 K, was obtained by fitting the data to a single-exponential decay curve. The single-exponential decay also confirms the single site of the  $Sm^{3+}$  environment in the crystals. There is no observable rising time associated with the lifetime of the  $^4G_{5/2}$  multiplet. This indicates that the lifetimes of the higher-lying multiplets are governed predominantly by fast nonradiative relaxation not measurable with the temporal resolution available in this work. Furthermore, we observed that the fluorescence lifetime of  $^4G_{5/2}$  is nearly temperature-independent. Even at room temperature, the fluorescence lifetime is  $24.29 \pm 0.01 \mu s$ . A further discussion of quantum efficiency is presented later in the section on JO calculation.

**C. Excitation Spectra.** In comparison with absorption spectroscopy, laser-induced fluorescence excitation spectroscopy has the advantage of selectivity. In many cases, it suppresses the inhomogeneous line broadening in electronic transitions and therefore provides higher resolution in probing the CF energy level structure. Figure 6 shows the excitation spectra of  $Sm^{3+}$  in  $Sm(Et_2Dtc)_3(bipy)$  at 77 K, which were obtained using a 5-ns pulse laser and monitoring the  $Sm^{3+}$  fluorescence from the  $^4G_{5/2}$  emitting state at 647.8 nm. In Figure 6a, two main peaks with a CF splitting of  $21 \text{ cm}^{-1}$  can be unequivocally assigned to excitation from the lowest level of  $^6H_{5/2}$  to the two CF levels of the  $^4F_{3/2}$  excited state. In Figure 6b, four CF levels of  $^4G_{7/2}$  can be clearly identified. In Figure 6c, five CF levels of  $^4I_{9/2}$  are identified. However, only part of the  $^4M_{15/2} + ^4I_{11/2}$  multiplets (3 levels) can be clearly resolved because of the very weak laser power in the blue region. All of these CF levels identified from the excitation spectra are listed in Table 1. The hot bands marked by arrows at the long-wavelength side in Figure 6a–c originate from the other two upper levels of the  $^6H_{5/2}$  ground state. According to the excitation spectra, the two upper CF levels of  $^6H_{5/2}$  were observed at  $\sim 59$  and  $106 \text{ cm}^{-1}$ , respectively, which is in good agreement with the assignment based on the emission spectra.

#### IV. Crystal-Field Analysis

So far, 57 CF levels have been identified based on the emission, excitation, and absorption spectra, as shown in Table 1. Generally, the CF splitting can be well interpreted by parametrization of an effective operator Hamiltonian including CF and FI interactions. The commonly used effective operator Hamiltonian is

$$H = H_{FI} + H_{CF} \quad (1)$$

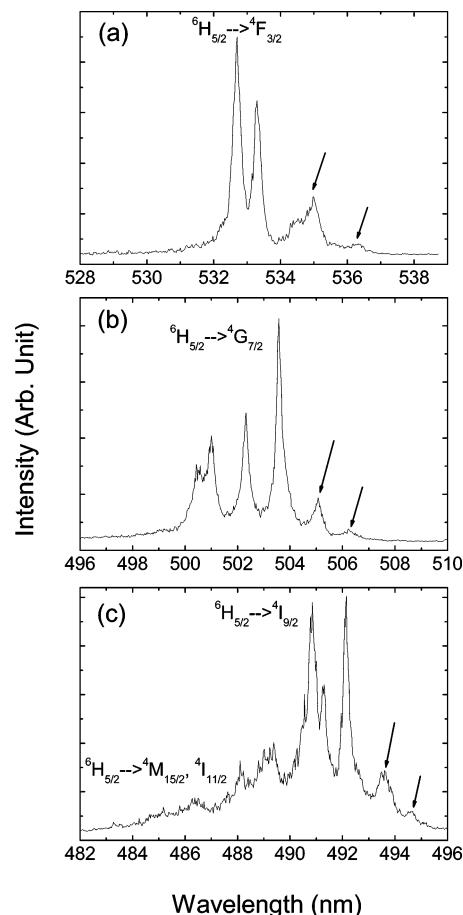


**Figure 6.** Excitation spectra of  $Sm^{3+}$  in  $Sm(Et_2Dtc)_3(bipy)$  crystals at 77 K, when pumped by a tunable dye laser in the wavelength range of (a) 528–539 nm; (b) 496–510 nm; and (c) 482–496 nm, respectively. The emission from the  $^4G_{5/2}$  manifold at 647.8 nm was monitored. The spectra were not calibrated for the laser power at different wavelengths, and the very weak bands observed near 482 nm were due to the rapid drop of laser power. The corresponding optical transitions are indicated above the lines, and lines marked by arrows are hot bands originating from the upper CF levels of  $^6H_{5/2}$ .

where the FI Hamiltonian can be expressed as

$$H_{FI} = E_{avg} + \sum_{k=2,4,6} F^k f_k + \zeta_f A_{SO} + \alpha L(L+1) + \beta G(R_2) + \gamma G(R_7) + \sum_{i=2,3,4,6,7,8} T^i t_i + \sum_{h=0,2,4} M^h m_h + \sum_{f=2,4,6} P^f p_f \quad (2)$$

There are up to 20 FI parameters in eq 2. The predominant terms in this Hamiltonian are the electrostatic and spin–orbit interactions represented by parameters  $F^k$  and  $\zeta_f$ , which were varied freely in our least-squares fitting of the CF energy level structure. The remaining terms represent higher-order interactions that are required in order to accurately reproduce the energy level structure of f-element ions. The configuration interactions ( $\alpha$ ,  $\beta$ ,  $\gamma$ ), spin–spin, and spin–other-orbit interactions ( $M^h$ ); the two-body electrostatically correlated magnetic interactions ( $P^f$ ); and the three-particle configuration interactions ( $T^i$ ) were fixed at the values obtained previously from analysis of  $Sm^{3+}:LaF_3$ .<sup>13</sup> The physical meaning of those FI parameters have been described by Carnell et al.<sup>13</sup>

The single-particle CF Hamiltonian is usually expressed in Wybourne's notation in which the specific number of CF parameters is determined by site symmetry.<sup>14</sup> Assuming the

**TABLE 2: FI and CF Parameters (cm<sup>-1</sup>) of Sm<sup>3+</sup> in the Sm(Et<sub>2</sub>Dtc)<sub>3</sub>(bipy) Crystal, Which Were Obtained from Fitting the Experimental Data Based on an Assumption of D<sub>2d</sub> Site Symmetry<sup>a</sup>**

parameter <sup>b</sup>	D <sub>2d</sub>
$E_{\text{avg}}$	47 011(40)
$F^2$	78 206 (145)
$F^4$	56 102(137)
$F^6$	40 215(84)
$\xi$	1168(2)
$B_0^2$	-263(37)
$B_0^4$	354(109)
$B_4^4$	301(63)
$B_0^6$	540(82)
$B_4^6$	-523(58)
rms <sup>c</sup>	17.3

<sup>a</sup> Values in parentheses are errors in the indicated parameters. <sup>b</sup> The  $\alpha$ ,  $\beta$ ,  $\gamma$ ,  $T^i$  ( $i = 2, 3, 4, 5, 6, 7, 8$ ),  $M^j$  ( $j = 0, 2, 4$ ), and  $P^k$  ( $k = 2, 4, 6$ ) parameters were kept the same as those in the Sm<sup>3+</sup>:LaF<sub>3</sub> crystals during the fitting procedure at the following values:  $\alpha = 20.16$ ,  $\beta = -566.9$ ,  $\gamma = 1500$ ;  $T^2 = 300$ ,  $T^3 = 36$ ,  $T^4 = 56$ ,  $T^6 = -347$ ,  $T^7 = 373$ ,  $T^8 = 348$ ;  $M^0 = 2.6$ ,  $M^2/M^0 = 0.56$ ,  $M^4/M^0 = 0.31$ ;  $P^2 = 357$ ,  $P^4/P^2 = 0.5$ ,  $P^6/P^2 = 0.1$ . <sup>c</sup> The root-mean-square (rms) deviation between the experimental and calculated energies was used as a figure of merit to describe the quality of a fit, with  $\text{rms} = \sqrt{\sum (E_{\text{exptl}} - E_{\text{calcd}})^2 / (N - P)}$ , where  $N = 57$ , the number of levels fit, and  $P = 10$ , the number of parameters freely varied.

Sm<sup>3+</sup> ions occupy sites of D<sub>2d</sub> symmetry in the lattice, we have

$$H_{\text{CF}} = B_0^2 C_0^{(2)} + B_0^4 C_0^{(4)} + B_0^6 C_0^{(6)} + B_4^4 (C_4^{(4)} + C_{-4}^{(4)}) + B_4^6 (C_4^{(6)} + C_{-4}^{(6)}) \quad (3)$$

Obviously, this is a very rough approximation because the assumed symmetry is higher than the actual site symmetry of C<sub>1</sub>. However, this approximation significantly reduces the number of CF parameters from 27 to 5, enabling practical CF energy-level fitting.

Theoretically, the 4f<sup>5</sup> configuration consists of 1001 twofold degenerate electronic states. Nowadays it is a very easy task to perform the complete diagonalization without truncation of the 4f<sup>5</sup> wave functions. In this work, the energy-level fitting was performed using an *f*-shell parametrization program with the corresponding CF parameters of the LaF<sub>3</sub>:Sm<sup>3+</sup> crystal<sup>13</sup> used as starting values. Fifty-seven levels of Sm<sup>3+</sup> in Sm(Et<sub>2</sub>Dtc)<sub>3</sub>(bipy) were fitted to 10 free parameters. The fitted energy levels below 25 000 cm<sup>-1</sup> are compared with the experimental values in Table 1. Table 2 lists the final FI and CF parameters of the fit. The root-mean-square (rms) deviation of the fit is 17.3 cm<sup>-1</sup>, which is reasonable given that the fitting was performed based on D<sub>2d</sub> instead of the actual C<sub>1</sub> site symmetry.

As seen in Table 1, the largest discrepancy is found at the lowest CF level of <sup>4</sup>G<sub>5/2</sub>, a difference of 54 cm<sup>-1</sup> between the calculated and the observed values. This discrepancy could be resolved by including additional mechanisms or parameters in the CF parametrization. Although the energy levels of <sup>6</sup>F<sub>1/2</sub>, <sup>6</sup>H<sub>15/2</sub>, and <sup>6</sup>F<sub>3/2</sub> are very close to each other, mixing of the free-ion wave functions is not strong. In fact, according to the wave functions obtained from the fitting, the term of <sup>6</sup>F<sub>1/2</sub> is very pure (96%) with negligible J-mixing, and about 7–9% of the components of <sup>6</sup>H<sub>15/2</sub> are mixed into the wave function of the CF level of <sup>6</sup>F<sub>3/2</sub>.

As we mentioned previously in Figure 2a, two relatively strong absorption bands were observed at 23 264 and 23 883 cm<sup>-1</sup> and tentatively assigned to (<sup>4</sup>M<sub>17/2</sub>, <sup>4</sup>G<sub>9/2</sub>, <sup>4</sup>I<sub>15/2</sub>) and (<sup>6</sup>P<sub>5/2</sub>,

**TABLE 3: CF Strengths of Sm<sup>3+</sup> Ions in Different Hosts**

host	symmetry	$S$ (cm <sup>-1</sup> )	ref
LaF <sub>3</sub>	$C_{2v}$	336	13
Y <sub>2</sub> O <sub>3</sub>	$C_2$	676	18
YAG	$D_2$	698	24
LiYF <sub>4</sub>	$D_{2d}$	370	30
Si <sub>5</sub> (PO <sub>4</sub> ) <sub>3</sub> F	$C_s$	851	31
GaN	$C_{3v}$	234	31
Sm(C <sub>5</sub> H <sub>4</sub> tBu) <sub>3</sub>	$D_{3h}$	1010	19
Sm(Cp)(Tp <sup>Me2</sup> ) <sub>2</sub>	$D_{5h}$	301	19
Sm(C <sub>5</sub> H <sub>4</sub> tBu) <sub>3</sub> (THF)	$C_{3v}$	792	19
Sm(Cp) <sub>3</sub> (THF)	$C_{3v}$	796	19
Sm(Cp) <sub>3</sub> (CNC <sub>6</sub> H <sub>11</sub> )	$C_{3v}$	793	19
Sm(Et <sub>2</sub> Dtc) <sub>3</sub> (bipy)	$D_{2d}$	194	this work

<sup>4</sup>M<sub>19/2</sub>), respectively. However, our fitting results suggest that there is only a small energy gap between the highest CF level of <sup>4</sup>M<sub>17/2</sub>, <sup>4</sup>G<sub>9/2</sub>, and <sup>4</sup>I<sub>15/2</sub> (22 868 cm<sup>-1</sup>) and the lowest CF level of <sup>6</sup>P<sub>5/2</sub> (23 642 cm<sup>-1</sup>). There is no matching level for the peak at 23 264 cm<sup>-1</sup>. Although there are some CF levels of <sup>4</sup>M<sub>19/2</sub> matching the peak at 23 883 cm<sup>-1</sup>, this assignment is still questionable because the absorption line intensity from the <sup>6</sup>H<sub>5/2</sub> ground state to <sup>4</sup>M<sub>19/2</sub> is expected to be very weak because it is strictly forbidden in the solution or free-ion state but weakly allowed by the very small contribution from the CF-induced J-mixing in the crystal. Consequently, we excluded these suspicious levels in the fit. A possible explanation for the unusually strong transition intensities and energy level discrepancy is that these multiplets are very close to the edge of the metal–ligand CT band and may borrow intensity from the neighboring CT band, which has the opposite parity. In this case, an accurate description of the energy level structure above 23 000 cm<sup>-1</sup> requires consideration of the excited charge transfer states.

In Table 1, we notice a significant red shift of the <sup>4</sup>G<sub>5/2</sub> multiplet (center of gravity at 17 797 cm<sup>-1</sup>), compared with aqueous Sm<sup>3+</sup> (17 900 cm<sup>-1</sup>),<sup>15</sup> Sm<sup>3+</sup>:LaF<sub>3</sub> (17 951 cm<sup>-1</sup>),<sup>16</sup> or Sm<sup>3+</sup>:SFAP (18 045 cm<sup>-1</sup>).<sup>17</sup> This shift is caused by the CF-induced nephelauxetic (electron cloud-expanding) effect, which is possibly related to the covalence in the Sm<sup>3+</sup>–ligand bond. Similarly, the position of the <sup>6</sup>F<sub>1/2</sub> multiplet (6245 cm<sup>-1</sup>) is also significantly red-shifted in comparison with the aqueous Sm<sup>3+</sup> (6400 cm<sup>-1</sup>)<sup>15</sup> or Sm<sup>3+</sup>:SFAP (6471 cm<sup>-1</sup>).<sup>17</sup>

The scalar CF strength ( $S$ ) that reflects the overall CF interaction in the crystal is calculated to be 194 cm<sup>-1</sup>, according to Chang's definition<sup>18</sup>

$$S = \left( \frac{1}{3} \sum_{k=2,4,6} \frac{1}{2k+1} \sum_q |B_q^k|^2 \right)^{1/2} \quad (4)$$

Table 3 compares the CF strengths of Sm<sup>3+</sup> ions in some common inorganic crystals as well as organic complexes, which were calculated based on the reported CF parameters in those hosts. (Note that the global CF strengths defined in ref 19 have been converted to  $S$  by dividing a factor of  $\sqrt{3}$ ). The CF strength of the Sm(Et<sub>2</sub>Dtc)<sub>3</sub>(bipy) crystal is the lowest among those reported in Table 3, indicating a very weak CF experienced by the Sm<sup>3+</sup> central ion.

The weak CF strength reflects the large distance between the Sm<sup>3+</sup> ion and its first-layer ligands. In Sm(Et<sub>2</sub>Dtc)<sub>3</sub>(bipy), the average Sm–S distance,  $R(\text{Sm}, \text{S})$ , is 0.286 nm, and  $R(\text{Sm}, \text{N})$  is 0.262 nm.<sup>11</sup> This is in contrast with  $R(\text{Sm}, \text{C})$  of 0.274 nm and  $R(\text{Sm}, \text{O})$  of 0.252 nm for Sm<sup>3+</sup> in Sm(Cp)<sub>3</sub>(THF)<sup>20</sup> or the  $R(\text{Sm}, \text{O})$  of 0.23 nm for Sm<sup>3+</sup> in YAG. For the crystal field interaction expressed in eq 3, the contributions of the rank-4

and rank-6 CF terms are from short-range interactions. Increasing of the ion–ligand distance results in less contribution from the short-range CF interactions, whereas the rank-2 CF components, namely, the  $B_q^2$  terms in eq 3, are less distance-dependent, and therefore, they account for more contribution to the CF splittings observed in this system.

### V. Judd–Ofelt Intensity Calculation

From the RT absorption spectrum of the Sm(Et<sub>2</sub>Dtc)<sub>3</sub>(bipy) pellet, the ratios of the integrated absorbance for the six IR absorption bands in Figure 2b can be obtained readily by simple integration. In our calculation, we assume that these intensity ratios remain unchanged for the chloroform solution of Sm(Et<sub>2</sub>Dtc)<sub>3</sub>(bipy) crystals. In other words, the JO intensity parameters ( $\Omega_{2,4,6}$ ) are assumed to be the same in both the bulk crystals and the chloroform solution. The above assumption is justified if the molecular structure of the nearest neighboring atoms/ions around the Sm<sup>3+</sup> central ion change little in the chloroform solution. To calculate the JO intensity parameters quantitatively,<sup>21,22</sup> we recorded the RT absorption spectrum of the chloroform solution containing Sm(Et<sub>2</sub>Dtc)<sub>3</sub>(bipy) of known Sm<sup>3+</sup> concentration, and part of it is shown in Figure 2c. Note that fundamental IR vibrations as well as binary and ternary combination vibrations and overtones of some organic groups (such as C–H and bipyridyl) in the solution interfered severely. Figure 2c shows only the IR absorption to <sup>6</sup>F<sub>11/2</sub>, <sup>6</sup>F<sub>9/2</sub>, and <sup>6</sup>F<sub>7/2</sub>. The ratios of the integrated absorbance for these three bands change little for Sm<sup>3+</sup> ions in either the solution or the pellet, confirming the assumption above. The integrated absorbance for the <sup>6</sup>F<sub>7/2</sub> band was calculated directly from Figure 2c, whereas those for the other five bands were obtained using the corresponding ratios.

The measured absorption line strengths,  $S_{\text{mea}}$ , from the ground <sup>6</sup>H<sub>5/2</sub> manifold ( $J = 5/2$ ) to the excited  $J'$  manifold can be obtained using the following expression<sup>23,24</sup>

$$S_{\text{mea}}(J \rightarrow J') = \frac{3ch(2J+1)}{8\pi^3 n_{\text{Sm}} \bar{\lambda} e^2} \frac{9n}{(n^2+2)^2} \Gamma \quad (5)$$

where  $n_{\text{Sm}}$  is Sm<sup>3+</sup> concentration in the chloroform solution ( $n_{\text{Sm}} = 4.080 \times 10^{17} \text{ cm}^{-3}$ ),  $n$  is the refractive index of the chloroform solution ( $n = 1.4460$ ),  $\bar{\lambda}$  is the mean wavelength of the absorption band, and  $\Gamma$  is the integrated absorbance for each absorption band, which can be expressed as

$$\Gamma = \frac{\ln 10}{L} \int_{J \rightarrow J'} \text{OD}(\lambda) d\lambda \quad (6)$$

where  $\text{OD}(\lambda)$  is the measured optical density as a function of wavelength and  $L$  is the optical path length ( $L = 5 \text{ cm}$ ). When two or more absorption bands overlapped, the total integrated absorbance of the bands was treated as a single experiment point. The excited  $J'$  manifolds included in the fit are <sup>6</sup>F<sub>11/2</sub>, <sup>6</sup>F<sub>9/2</sub>, <sup>6</sup>F<sub>7/2</sub>, <sup>6</sup>F<sub>5/2</sub>, <sup>6</sup>F<sub>3/2</sub>, and <sup>6</sup>F<sub>1/2</sub> + <sup>6</sup>H<sub>15/2</sub>. According to JO theory, the absorption line strength for electric-dipole (ED) transition can also be expressed in terms of  $\Omega_{2,4,6}$  parameters by<sup>24</sup>

$$S_{\text{calcd}}(J \rightarrow J') = \sum_{\tau=2,4,6} \Omega_{\tau} |\langle \Phi J || U^{(\tau)} || \Phi' J' \rangle|^2 \quad (7)$$

The reduced tensor matrix elements  $|\langle \Phi J || U^{(\tau)} || \Phi' J' \rangle|^2$  were calculated on the basis of the intermediate-coupling wave functions obtained from the energy-level fitting. By a least-

**TABLE 4: Measured and Calculated Absorption Line Strengths from <sup>6</sup>H<sub>5/2</sub> for the Chloroform Solution of Sm(Et<sub>2</sub>Dtc)<sub>3</sub>(bipy)<sup>a</sup>**

J manifold	$\bar{\lambda}$ (nm)	$S_{\text{mea}}$	$S_{\text{calcd}}$
<sup>6</sup> F <sub>11/2</sub>	964	0.137	0.101
<sup>6</sup> F <sub>9/2</sub>	1108	0.787	0.715
<sup>6</sup> F <sub>7/2</sub>	1264	1.151	1.213
<sup>6</sup> F <sub>5/2</sub>	1424	0.820	0.806
<sup>6</sup> F <sub>3/2</sub>	1535	0.612	0.589
<sup>6</sup> F <sub>1/2</sub> + <sup>6</sup> H <sub>15/2</sub>	1613	0.294	0.313
rms $\Delta S$ ( $10^{-20} \text{ cm}^2$ )			0.062
rms error			8.6%

<sup>a</sup>  $S_{\text{mea}}$  and  $S_{\text{calcd}}$  are in units of  $10^{-20} \text{ cm}^2$ .

squares fitting of  $S_{\text{calcd}}$  to the measured line strengths,  $S_{\text{mea}}$ , the three JO intensity  $\Omega_{2,4,6}$  parameters were obtained ( $\Omega_{2,4,6} = 1.57, 2.65$ , and  $3.65$ , in units of  $10^{-20} \text{ cm}^{-1}$ ). The values of the measured and calculated line strengths are listed in Table 4. The rms deviation between the experimental and calculated line strengths is defined by<sup>24</sup>

$$\text{rms}\Delta S = \sqrt{\sum_{i=1}^N (S_{\text{mea}} - S_{\text{calcd}})^2 / (N-3)} \quad (8)$$

where  $N$  is the number of absorption bands. A measurement of the relative error is given by the rms error =  $\text{rms}\Delta S / \text{rms}S \times 100\%$ , where  $\text{rms}S = \sqrt{\sum_{i=1}^N S_{\text{mea}}^2 / N}$ . The values of  $\text{rms}\Delta S$  and the rms error are also presented in Table 4. The rms error of the fitting is 8.6%, which indicates that the fitting results are in good agreement with the experiments.

Once the JO intensity parameters are determined, the ED radiative transition rate  $A(J \rightarrow J')$  in the crystal, corresponding to transitions from <sup>4</sup>G<sub>5/2</sub> to the lower manifolds <sup>6</sup>H <sub>$J$</sub>  ( $J = 5/2, 7/2, 9/2, 11/2, 13/2$ , and  $15/2$ ) and <sup>6</sup>F <sub>$J$</sub>  ( $J = 1/2, 3/2, 5/2, 7/2, 9/2$ , and  $11/2$ ), can be calculated by the following equation<sup>23,24</sup>

$$A(J \rightarrow J') = \frac{64\pi^4 e^2}{3h(2J+1)\bar{\lambda}^3} \frac{n(n^2+2)^2}{9} \sum_{\tau=2,4,6} \Omega_{\tau} |\langle [^4G_{5/2}] || U^{(\tau)} || [^6L_J] \rangle|^2 \quad (9)$$

where  $n$  is the crystal refractive index, and the values of  $|\langle [^4G_{5/2}] || U^{(\tau)} || [^6L_J] \rangle|^2$  are calculated based on the intermediate-coupling wave functions obtained from the energy-level fitting. Because the crystal refractive index of Sm(Et<sub>2</sub>Dtc)<sub>3</sub>(bipy) is not known, an assumed value of 1.9 was used in the calculation. Therefore, the radiative lifetime and branching ratios from <sup>4</sup>G<sub>5/2</sub> can be estimated from the relations

$$\tau_r = \frac{1}{\sum_{J'} A(J \rightarrow J')} \quad \text{and} \quad \beta_{J \rightarrow J'} = \frac{A(J \rightarrow J')}{\sum_{J'} A(J \rightarrow J')}$$

The radiative quantum efficiency is defined as the following:  $\eta = \tau_f / \tau_r$ , where  $\tau_f$  is the fluorescence lifetime. The calculated radiative transition rates and branching ratios are listed in Table 5.

The calculated radiative lifetime and quantum efficiency for the crystals at RT are 3.24 ms and 0.75%, respectively. The corresponding nonradiative transition rate at RT ( $\tau_r^{-1} - \tau_f^{-1}$ ) is estimated to be  $4.08 \times 10^4 \text{ s}^{-1}$ . Because the fluorescence lifetime is nearly temperature-independent, the quantum efficiency and nonradiative transition rate are also independent of temperature. This dynamic behavior can be explained well in view of the

**TABLE 5: Calculated Branching Ratios and Radiative Transition Rates for the Emissions from  $^4G_{5/2}$  to the Lower Manifolds at RT**

manifold	$\bar{\lambda}$ (nm)	$\beta$ (%)		$A$ ( $s^{-1}$ )
		obs <sup>a</sup>	calcd	
$^6H_{5/2}$	565.4	4.8	3.3	10
$^6H_{7/2}$	604.1	32.5	41.1	127
$^6H_{9/2}$	647.85	47.1	34.0	105
$^6H_{11/2}$	707	10.0	11.9	37
$^6H_{13/2}$	786.4	4.7	1.6	5.0
$^6F_{1/2}$	874	0.8	0.59	1.8
$^6H_{15/2}$	882.5		0.05	0.17
$^6F_{3/2}$	885.4		0.67	2.1
$^6F_{5/2}$	927.6		4.6	14
$^6F_{7/2}$	1007		1.2	3.6
$^6F_{9/2}$	1138		0.70	2.1
$^6F_{11/2}$	1348		0.11	0.34

<sup>a</sup> According to the calibrated fluorescence spectra at RT.

multiphonon relaxation mechanism. The multiphonon relaxation rate can be expressed as<sup>25,26</sup>

$$A_{\text{nonrad}} = A_0[1 - \exp(-\hbar\omega/kT)]^{-N} \quad (10)$$

where  $N$  is the number of phonons with the frequency of  $\omega$  that are required to bridge the energy gap between the  $^4G_{5/2}$  and the next-highest-energy multiplet ( $^6F_{11/2}$ ) ( $\sim 7500 \text{ cm}^{-1}$ ). If high-energy phonon modes (such as high-frequency localized vibrational modes) are involved, then the number of phonons needed would be small. For example, in  $\text{Sm}(\text{Et}_2\text{Dtc})_3(\text{bipy})$  crystals, the IR mode from the bipyridyl group can be as high as  $3055 \text{ cm}^{-1}$ .<sup>8</sup> Less than three phonons of this kind of mode can effectively bridge the energy gap. Therefore, a very fast multiphonon relaxation could lead to the very low quantum efficiency we observed. Furthermore, with phonons of high frequencies, the multiphonon relaxation rate expressed in eq 10 is almost a constant from liquid helium to room temperature.

As seen in Table 5, the largest calculated branching ratio is for the transition to  $^6H_{7/2}$  instead of to  $^6H_{9/2}$  as we observed. However, the overall agreement between the calculated and the measured branching ratios for the emissions from  $^4G_{5/2}$  to the lower manifolds is reasonable, if one keeps in mind that the error for JO calculation can be up to 30%. In our case, the three CF levels of  $^4G_{5/2}$  (17 687, +145, +187  $\text{cm}^{-1}$ ) are definitely not equally populated at RT.

## VI. Thermal Line Broadening and Shifts

The thermal line broadening and shifts of optical transitions in solids provide valuable information on electron–phonon interactions and lattice dynamics. The contributions to experimentally measured line widths generally come from inhomogeneous crystalline defects, and direct one-phonon and multiphonon processes including Raman phonon scattering. In the crystals we studied, the emission from the lowest CF level of  $^4G_{5/2}$  to  $^6F_{1/2}$  (Figure 4e) is the strongest but has the narrowest line width at 77 K, compared to those hot bands or transitions terminating at the  $^6H_{15/2}$  or  $^6F_{3/2}$  multiplets. This fact can be understood easily because there are no spontaneous one-phonon emission processes possible for both  $^4G_{5/2}(1)$  and  $^6F_{1/2}$  doublets, as there are for the other transitions. In addition, this line is well separated from the other lines. Therefore, it is a good candidate for studying the effect of line broadening and shifts. The  $^4G_{5/2}(1) \rightarrow ^6F_{1/2}$  line was observed to have a nearly Lorentzian shape at temperatures from 77 to 300 K. Thus, we assume that Raman phonon scattering processes play a leading

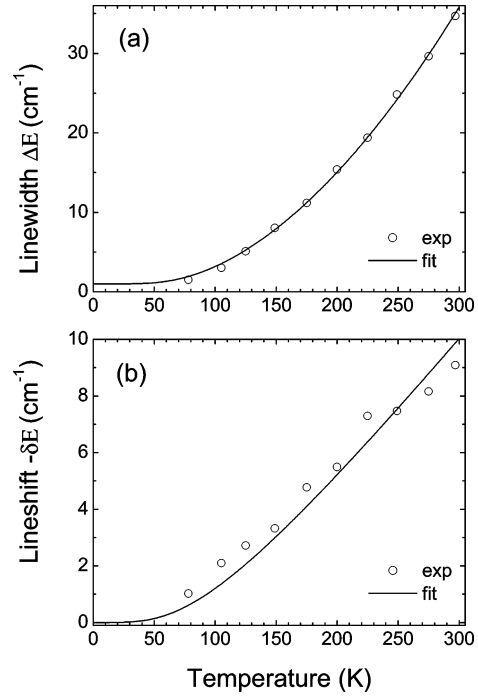


**Figure 7.** Model fitting of the experimental data to (a) thermal line broadening and (b) line shifts of the  $^4G_{5/2}(1) \rightarrow ^6F_{1/2}$  transition. The results suggest that ion-phonon interaction in the  $\text{Sm}(\text{Et}_2\text{Dtc})_3(\text{bipy})$  crystals agree with the McCumber–Sturge theoretical model described in the text.

role for the line broadening and we neglect the one-phonon absorption and multiphonon processes. The observed thermal line width and line shifts are shown in Figure 7a and b, respectively. The observed line width data have been calibrated by subtracting the instrumental line width, whereas part of the line width is the contribution from inhomogeneous broadening.

Theoretically, the temperature-dependent line width ( $\Delta E$ ) and line shifts ( $\delta E$ ) associated with two levels of the optical transition can be expressed, respectively, by the McCumber–Sturge equations<sup>27,28</sup>

$$\Delta E(\text{cm}^{-1}) = \Delta E_0 + \bar{\alpha} \left( \frac{T}{T_D} \right)^7 \int_0^{T_D/T} \frac{x^6 e^x}{(e^x - 1)^2} dx \quad (11)$$

and

$$\delta E(\text{cm}^{-1}) = \alpha \left( \frac{T}{T_D} \right)^4 \int_0^{T_D/T} \frac{x^3}{e^x - 1} dx$$

where  $\Delta E_0$  is the residual width from the two levels, temperature independent, and due to random crystal strains;  $\bar{\alpha}$  and  $\alpha$  are the coupling coefficients for the electron–phonon interaction; and  $T_D$  is the effective Debye temperature of the phonon distribution.  $\bar{\alpha}$ ,  $\alpha$ , and  $T_D$  are treated as adjustable parameters to get the best fit to the experimental data. The physical meaning for the above parameters has been described previously.<sup>28</sup> The residual width and line position at  $T = 0 \text{ K}$  were estimated by extrapolating the experimental data to zero temperature, where  $\Delta E_0 = 1.0 \text{ cm}^{-1}$ . The fitted curves and experimental data are shown in Figure 7a and b. As can be seen from Figure 7, the line width fitting is good, and the line shift fitting is reasonable, noting that only three parameters used in the fit and  $T_D$  are shared by both equations. These facts may justify our assumption that the Raman phonon scattering processes are responsible for the thermal line broadening and shifts we observed. The fitting



values of  $\bar{\alpha}$ ,  $\alpha$ , and  $T_D$  are 255 cm<sup>-1</sup>, -55.5 cm<sup>-1</sup>, and 350 K, respectively. According to a large number of experimental line-broadening data on rare-earth doped LiYF<sub>4</sub> crystals, Ellens et al. concluded that the electron-phonon coupling strength is large at the beginning (Ce<sup>3+</sup>, Pr<sup>3+</sup>, Nd<sup>3+</sup>) and the end (Er<sup>3+</sup>, Tm<sup>3+</sup>, Yb<sup>3+</sup>) of the trivalent lanthanide-ion series, but small at the center (Eu<sup>3+</sup>, Gd<sup>3+</sup>, Tb<sup>3+</sup>).<sup>29</sup> The electron-phonon coupling strength of Sm<sup>3+</sup> is thus expected to be small. In fact, the value of  $\bar{\alpha}$  for Sm<sup>3+</sup> is interpolated to be less than 100 cm<sup>-1</sup> based on the trend observed.<sup>29</sup> Obviously, the fitted value of  $\bar{\alpha}$  for Sm<sup>3+</sup> in Sm(Et<sub>2</sub>Dtc)<sub>3</sub>(bipy) crystals is much larger than that for Sm<sup>3+</sup>:LiYF<sub>4</sub>, which is quite possibly due to the much lower opposite parity states (CT states) in the former lattices. As pointed out by Ellens et al., the lower the energy of the opposite parity states, the more these states will be admixed in the 4f<sup>n</sup> states, which gives an increase in the electron-phonon coupling strength.<sup>29</sup> This usually happens to rare-earth ions doped in more covalent lattices. The negative sign of  $\alpha$  means that, when temperature goes up, the line shifts to the red. The Debye temperature obtained in this work needs to be further confirmed by future experiments such as heat capacity measurement.

## VII. Conclusions

We have conducted detailed analyses of crystal-field energy level structure and excited-state dynamics of Sm<sup>3+</sup> in the mixed-ligand crystal of Sm(Et<sub>2</sub>Dtc)<sub>3</sub>(bipy) based on experimental data from absorption, laser excitation, and fluorescence measurements. These analyses have provided insights into the electronic and chemical properties of f-elements in this series of soft-ligand compounds that are currently lacking fundamental understanding. A crystal-field analysis of the 57 experimental energy levels of Sm<sup>3+</sup> gives a good account of the experimental data with model  $D_{2d}$  symmetry instead of the actual  $C_1$  site symmetry. The Sm<sup>3+</sup> ions in the lattice experience a rather weak CF environment based on the CF parameters obtained from the fit. JO intensity calculation has been conducted successfully to obtain the three intensity parameters as well as other spectroscopic parameters that characterize the lattice dynamics. The calculated radiative lifetime from the <sup>4</sup>G<sub>5/2</sub> manifold is about 3.24 ms, much longer than the observed fluorescence lifetime of 24.5  $\mu$ s. The fluorescence quantum efficiency (0.75%) is thus extremely low, which is quite possibly due to the existence of very efficient multiphonon relaxation processes induced by the high-frequency localized vibrational modes in the bipyridyl group. The calculated branching ratios for transitions from the <sup>4</sup>G<sub>5/2</sub> manifold are in agreement with the measured values obtained from the RT emission spectrum. Furthermore, it is shown that Raman phonon scattering processes are responsible for the thermal line broadening and shifts of the <sup>4</sup>G<sub>5/2</sub>(1)  $\rightarrow$  <sup>6</sup>F<sub>1/2</sub> transition we observed, according to the good fit to the McCumber-Sturge equations. The coupling strength for the electron-phonon interaction and Debye temperature was also reported. It is noticed that the CF model does not provide a good fit to the energy levels above 20 000 cm<sup>-1</sup>, whereas the relative intensities of the absorption spectrum in the same region

do not agree with the JO calculation. The ligand-Sm<sup>3+</sup> charge-transfer transition that occurs at energy levels above 22 000 cm<sup>-1</sup> should strongly influence the 4f states with energy levels in the same region and therefore induce significant covalence in this system.

**Acknowledgment.** Work at Argonne National Laboratory was performed under the auspices of the Office of Basic Energy Science, Division of Chemical Sciences, U.S. Department of Energy, under Contract no. W-31-109-ENG-38. The authors are grateful to M. F. Reid for the f-shell empirical modeling program.

## References and Notes

- (1) Nash, K. L. *Solvent Extr. Ion Exch.* **1993**, *11*, 729.
- (2) Iveson, P. B.; Rivière, C.; Guillauneux, D.; Nierlich, M.; Thuéry, P.; Ephritikhine, M.; Madic, C. *Chem. Commun.* **2001**, 1512.
- (3) Jensen, M. P.; Bond, A. H. *J. Am. Chem. Soc.* **2002**, *124*, 9870.
- (4) Berthet, J.-C.; Miquel, Y.; Iveson, P. B.; Nierlich, M.; Thuéry, P.; Madic, C.; Ephritikhine, M. *J. Chem. Soc., Dalton Trans.* **2002**, 3265.
- (5) Berthet, J.-C.; Rivière, C.; Miquel, Y.; Nierlich, M.; Madic, C.; Ephritikhine, M. *Eur. J. Inorg. Chem.* **2002**, 1439.
- (6) Zhu, Y.; Chen, J.; Jiao, R. *Solvent Extr. Ion Exch.* **1996**, *14*, 61.
- (7) Miguiditchian, M.; Guillauneux, D.; Guillaumont, D.; Moisy, P.; Madic, C.; Jensen, M. P.; Nash, K. L. *Inorg. Chem.* **2005**, *44*, 1404.
- (8) Su, C.; Tang, N.; Tan, M.; Yu, K. *Polyhedron* **1996**, *15*, 233.
- (9) Hitchcock, P. B.; Hulkes, A. G.; Lappert, M. F.; Li, Z. *Dalton Trans.* **2004**, 129.
- (10) Bower, J. F.; Cotton, S. A.; Fawcett, J.; Hughes, R. S.; Russell, D. R. *Polyhedron* **2003**, *22*, 347.
- (11) Varand, V. L.; Glinskaya, L. A.; Klevtsova, R. F.; Larionov, S. V. *J. Struct. Chem.* **2000**, *41*, 544.
- (12) Varand, V. L.; Glinskaya, L. A.; Klevtsova, R. F.; Larionov, S. V. *J. Struct. Chem.* **1998**, *39*, 244.
- (13) Carnall, W. T.; Goodman, G. L.; Rajnak, K.; Rana, R. S. *J. Chem. Phys.* **1989**, *90*, 3443.
- (14) Wybourne, B. G. *Spectroscopic Properties of Rare Earths*; Interscience: New York, 1965.
- (15) Carnall, W. T.; Fields, P. R.; Rajnak, K. *J. Chem. Phys.* **1968**, *49*, 4412.
- (16) Carnall, W. T.; Goodman, G. L.; Rajnak, K.; Rana, R. S. *A Systematic Analysis of the Spectra of the Lanthanides Doped into Single-Crystal LaF<sub>3</sub>*; Argonne National Laboratory Report no. ANL-88-8; Argonne, Illinois, 1988.
- (17) Gruber, J. B.; Zandi, B.; Ferry, M.; Merkle, L. D. *J. Appl. Phys.* **1999**, *86*, 4377.
- (18) Chang, N. C.; Gruber, J. B.; Leavitt, R. P.; Morrison, C. A. *J. Chem. Phys.* **1982**, *76*, 3877.
- (19) Amberger, H.-D.; Reddmann, H.; Jank, S.; Lopes, M. I.; Marques, N. *Eur. J. Inorg. Chem.* **2004**, 98.
- (20) Wang, S.; Yu, Y.; Ye, Z.; Qian, C. *J. Organomet. Chem.* **1994**, *464*, 55.
- (21) Judd, B. R. *Phys. Rev.* **1962**, *127*, 750.
- (22) Ofelt, G. S. *J. Chem. Phys.* **1962**, *37*, 511.
- (23) Krupke, W. F. *Phys. Rev.* **1966**, *145*, 325.
- (24) Krupke, W. F. *IEEE J. Quantum Electron.* **1971**, *7*, 153.
- (25) Riseberg, L. A.; Moos, H. W. *Phys. Rev.* **1968**, *174*, 429.
- (26) Weber, M. J. *Phys. Rev.* **1968**, *171*, 283.
- (27) McCumber, D. E.; Sturge, M. D. *J. Appl. Phys.* **1963**, *34*, 1682.
- (28) Chen, X.; Di Bartolo, B. J. *Lumin.* **1993**, *54*, 309.
- (29) Ellens, A.; Andres, H.; ter Heerdt, M. L. H.; Wegh, R. T.; Meijerink, A.; Blasse, G. *Phys. Rev. B* **1997**, *55*, 180.
- (30) Wells, J. P. R.; Yamaga, M.; Han, T. P. J.; Gallagher, H. G.; Honda, M. *Phys. Rev. B* **1999**, *60*, 3849.
- (31) Gruber, J. B.; Zandi, B.; Lozykowski, H. J.; Jadwisieniczak, W. M. *J. Appl. Phys.* **2002**, *91*, 2929.